CIMAC CONGRESS 25
ZURICH, MAY 19 – 23, 2025

2025 | 337

Pre-Chamber Strong Swirl Combustion Model for a Dual-Fuel Engine's Digital Twin System

Simulation Technologies, Digital Twins and Complex System Simulation

Xiao Han, Harbin Engineering University

Dai Liu, Harbin Engineering University
Long Liu, Harbin Engineering University
Qian Xia, China Shipbuilding Power Engineering Institute Co., Ltd.

ABSTRACT

Digital twin system could improve the research, development and maintenance of marine engines, with high accuracy models. Dual-fuel engines with low-pressure natural gas indicate the significant advantages of low modification cost and can meet IMO Tier III emission standards without any after-treatment devices or EGR. In large-bore low-speed dual-fuel engines, the interaction between in-cylinder swirl and pre-chamber jet flame dominates the combustion processes, which is key to constructing the strong swirl combustion models. In this regard, based on experimental data, this study conducts CFD simulations and through in-cylinder jet flame combustion observations, develops a reduced-dimension phenomenological model for the pre-chamber dual-fuel strong swirl combustion. The model incorporates a swirl dynamic model into the turbulent kinetic energy calculation, thereby improving the simulation of combustion under jet flame entrainment and turbulent entrainment mixing control. Validation results show that the model can predict the entrained mass, temperature, and pressure throughout the engine cycle quickly and accurately. Therefore, this digital twin model could help develop and optimize the synergistic effect of swirl and combustion in low-pressure dual-fuel low-speed engines.

1 INTRODUCTION

Low-pressure direct injection natural gas dual-fuel engines, due to their pre-chamber ignition system and premixed combustion, offer significant advantages such as high ignition energy and low emissions, allowing them to meet Tier III emission standards without the need for any after-treatment devices or EGR. However, the premixed combustion process, which is prone to issues such as knocking, severely hinders the improvement of engine power. Furthermore, the narrow combustion limits of natural gas affect the control of the engine's air-fuel ratio [1]. Therefore, it is essential to analyze the in-cylinder combustion process and its key influencing factors to perform performance simulation and optimization for combustion improvement and power enhancement.

In large-bore, low-speed, two-stroke dual-fuel engines, the value of the swirl ratio is much greater than that of the tumble ratio. While tumble plays a role in the mixing process of natural gas and air, its effect is significantly lower than that of swirl. During the scavenging and compression processes, swirl influences the mixing of natural gas and air [2-5]. A homogeneous premixed charge is the foundation for complete combustion, which directly affects the likelihood of knocking. After the compression process, the pilot fuel in the pre-chamber is deflected and diffused under the influence of swirl, and the pre-chamber jet in the main combustion chamber interacts with the swirl, affecting the flame propagation velocity and the charge motion, which in turn impacts combustion and emissions. Thus, swirl plays a crucial role in the combustion process of large-bore two-stroke low-speed engines [6].

In recent years, many researchers have conducted studies on this topic from different perspectives. Most of them have explored combustion mechanisms through simulation experiments or CFD simulations, with a focus on the impact of swirl flow on combustion. For example, Tunç et al. [7] investigated the effect of different swirl numbers on the combustion stability of fuel mixtures with different oxygen ratios under various conditions. Their results indicated that the swirl number has a significant impact on flame stability. Jeon et al. [8] studied the combustion and emission characteristics under different swirl chamber parameters and found that due to the strong swirl, OH* and CH* radicals are more concentrated in the corners of the flame, and as the swirl angle increases, the chemiluminescence intensity in the radial direction of the flame becomes stronger and broader. Hu et al. [9] investigated the formation of active pre-chamber jet flames based on airflow synergistic effects and found that pre-chambers with larger nozzle swirl angles can generate stronger swirls, thus accelerating the evaporation and mixing of nearby fuel. Lu et al. [10] enhanced in-cylinder gas disturbance by increasing the swirl ratio to improve ammonia combustion efficiency, reducing fuel attachment to the walls, and accelerating the formation of combustible mixtures, thereby optimizing combustion and improving engine performance. Ye et al. [11] used numerical simulations to study the effect of swirl ratio on the combustion process in low-speed two-stroke dual-fuel engines and found that faster swirl motion accelerated the movement of active species, leading to faster flame propagation and a larger combustion area. Wu et al. [12] studied the effect of swirl on flame jets and natural gas combustion by varying the swirl intensity while maintaining a constant equivalence ratio in the cylinder. Their results showed that swirl significantly accelerated the combustion rate of natural gas, increased the flame propagation speed, raised cylinder pressure, and reduced the combustion duration.

However, most of the above studies focus on adjusting the swirl by setting swirl ratios or changing structural parameters, without paying sufficient attention to the formation, morphology, flow characteristics, and influencing factors of the swirl itself. Additionally, CFD simulations take a long time, often requiring dozens of hours, and are more suitable for investigating in-cylinder flow details and performing local analysis. Given the high costs associated with shipborne low-speed engine experiments, and in response to increasingly stringent emission regulations and changing market demands, there is an urgent need to conduct basic performance simulations to discuss the impact of variable parameters on engine power, economy, and emissions. This calls for the application of digital twin technology to develop intelligent ships. Through ‘multiple digital iterations’ and ‘one successful real-world development process’, the quality and efficiency of low-speed engine R&D can be significantly improved [13-15]. Clearly, the current CFD simulations are not fast enough to meet the real-time requirements of digital twin models, so high-precision and high-speed low-dimensional physical models need to be proposed. In this regard, Liu et al. [16] conducted phenomenological modeling research on shipborne low-speed pre-chamber dual-fuel engines and considered the turbulence kinetic energy generated by the conversion of swirl kinetic energy in the calculation of turbulence kinetic energy. However, the calculation of swirl velocity was not detailed, and the component of jet velocity was temporarily used as a substitute.

Therefore, this paper focuses on shipborne pre-chamber low-pressure direct injection natural gas dual-fuel engines, and based on experimental data, develops a CFD model. By analyzing the results of the multi-physics model and observing the flame propagation phenomenon, a strong swirl combustion process model for pre-chamber dual-fuel engines is established. The relationship between initial turbulence kinetic energy and combustion process is also analyzed. The overall research methodology is shown in Figure 1.

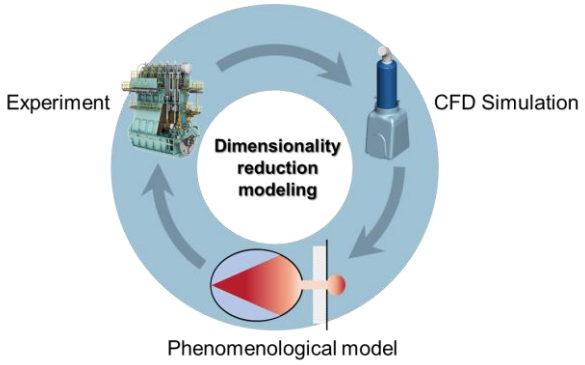

Figure 1. Schematic diagram of overall research ideas.

2 CONSTRUCTION AND ANALYSIS OF THE DUAL-FUEL ENGINE SIMULATION MODEL

2.1 CFD Simulation Model Construction and Validation

This study focuses on a shipborne pre-chamber low-pressure direct injection natural gas dual-fuel engine. A CFD model was established using 3D simulation software, including structures such as the exhaust port, exhaust valve, pre-chamber, cylinder, natural gas injection valve, and scavenging box, as shown in Figure 2. The model contains two pre-chambers, each equipped with an injector featuring three nozzles. The engine parameters at 75% load, including the structural and pilot fuel injection parameters, are shown in Table 1. The simulated calculation interval was set from the moment the exhaust valve opens (105°CA) to the moment the exhaust valve opens in the next cycle (465°CA), simulating one complete working cycle (360°CA). The calculated cylinder pressure from the simulation was compared with experimental data, as shown in Figure 3. The results are in good agreement, indicating that the model can accurately predict the actual operating process of the engine.

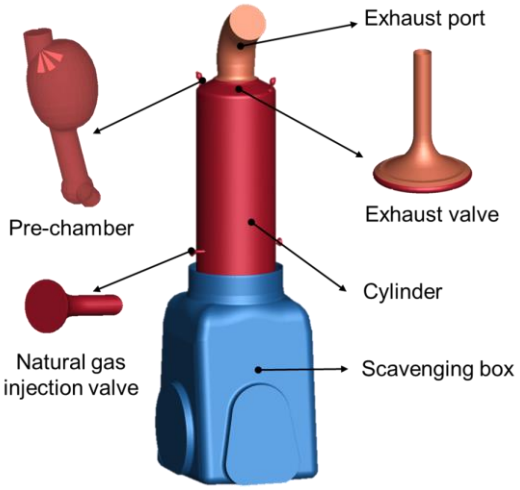

Figure 2. Schematic diagram of the 3D model of the dual-fuel engine.

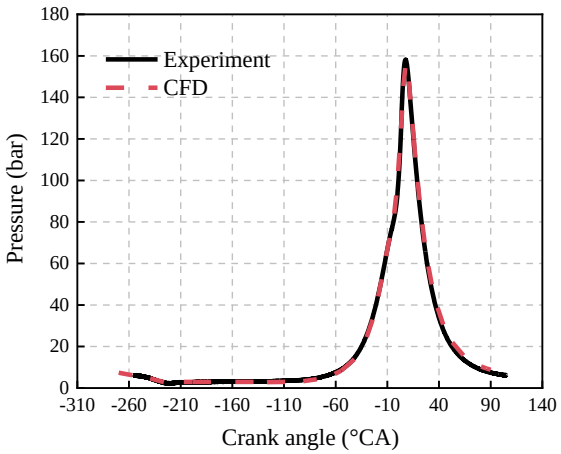

Figure 3. Comparison of experimental cylinder pressure and CFD simulation cylinder pressure results

Table 1. Engine specifications

Parameters	Value
Bore (mm)	920
Stroke (mm)	3468
Compression ratio	15.9
Speed (rpm)	72.7
Power (kW)	3545
SOI of natural gas (°CA)	235.5
Injection duration of natural gas (°CA)	13
Injection pressure of natural gas (bar)	11.4
Injection mass of natural gas (g)	111
SOI of pilot diesel (ATDC)(°CA)	-6.06
Injection duration of pilot diesel (°CA)	0.94
Injection pressure of pilot diesel (bar)	1200
Injection mass of pilot diesel (g)	0.69
Number of nozzles	3*2

2.2 Analysis of the Pre-Chamber Dual-Fuel Combustion Process

Through the simulation analysis of the post-processing results for the pre-chamber low-pressure direct injection natural gas engine, it can be concluded that during the compression process, natural gas and air are fully mixed under the influence of swirl, forming a relatively uniform premixed charge. A portion of this mixture enters the pre-chamber through the connecting passage near the top dead center. Before the top dead center, pilot fuel is injected into the pre-chamber by the injector. Under high-temperature, high-pressure conditions and the influence of the high-velocity rotating swirl, the premixed charge is continuously entrained and burned. The flame core gradually expands, and under the effect of pressure differential, the unburned mixture and the burning flame in the pre-chamber are ejected through the connecting passage, forming a jet flame that enters the main combustion chamber. This jet flame entrains the remaining unburned premixed charge in the main combustion chamber at high velocity, igniting it. The subsequent combustion is controlled by the entrainment of the jet flame and the swirl mixing in the main combustion chamber. A schematic diagram of the entire process is shown in Figure 4.

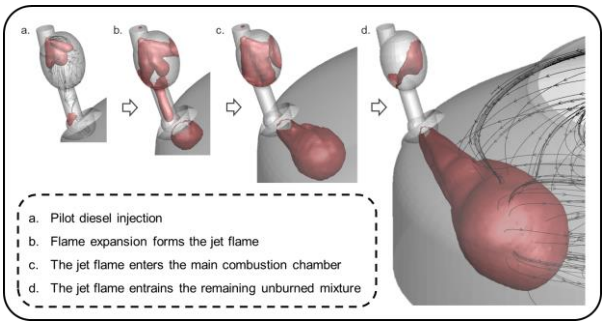

Figure 4. Schematic diagram of the strong swirl combustion process in the pre-chamber dual-fuel engine

3 PRE-CHAMBER JET FLAME STRONG SWIRL COMBUSTION PHENOMENOLOGICAL MODEL CONSTRUCTION

3.1 Model Overview

Based on the simulation analysis and observation of the combustion process in the pre-chamber low-pressure natural gas direct injection dual-fuel engine, a pre-chamber jet flame strong swirl combustion model is constructed in this paper. Figure 5 shows the schematic diagram of the model.

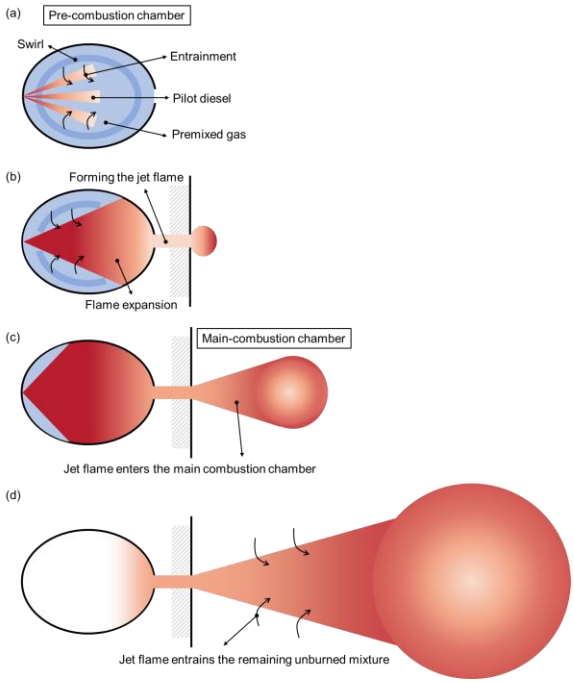

Figure 5. Schematic diagram of the pre-chamber dual-fuel strong swirl combustion model

In the modeling process, the combustion process in the pre-chamber is considered first. The model assumes that before the pilot fuel is injected, the pre-chamber is filled with a homogeneous mixture of natural gas and air. Subsequently, the pilot fuel is injected into the pre-chamber at high pressure, entraining the surrounding premixed charge and igniting it. Since the airflow is “compressed,” the pre-chamber is also filled with a high-speed rotating swirl. The flame formed by the combustion of pilot fuel and premixed charge rapidly expands in a conical shape, causing a sharp increase in temperature and pressure within the pre-chamber. Then, under the effect of pressure differential, the expanding flame forms a jet flame through the connecting passage and enters the main combustion chamber. Under the influence of the high-speed jet and the strong swirl in the main combustion chamber, the remaining premixed charge is entrained and ignited, completing combustion in the main combustion chamber. The pre-chamber jet flame is a form of multi-point ignition, with a large ignition area. It has a certain jet velocity in the early stage, while the jet velocity gradually decays in the later stage. Therefore, it is assumed that the jet flame propagates from the jet boundary to the surrounding area in a conical and spherical shape.

In the specific modeling process, the entire combustion process is divided into four parts: the pilot fuel ignition process, the pre-chamber combustion process, the jet flame ignition and entrainment process, and the turbulent

entrainment combustion process in the main combustion chamber. The pre-chamber and main combustion chamber are divided into two regions: the burned and unburned regions. The following model assumptions are made:

- The atomization and evaporation of the fuel are neglected, and the fuel develops as a gas-phase jet.
- Each region is considered independent, while satisfying overall mass and energy conservation, and the sum of the volumes of all regions equals the total volume.
- The mixture behaves according to the ideal gas law, and the gas composition in the unburned region remains unchanged.
- The pressures in each of the two regions within the pre-chamber and the main combustion chamber are assumed to be equal.

3.2 Model Construction

3.2.1 Pilot Fuel Ignition Process

1) The outlet velocity of the pilot fuel, v_{oil}, can be derived from the Bernoulli equation, as shown in Equation 1.

$$v_{oil} = \sqrt{\frac{2 \cdot \left(P_{id} - P_{pc}\right)}{\rho_{oil}}} \tag{1}$$

Where P_{id} is the pilot fuel injection pressure, P_{pc} is the pre-chamber pressure, and ρ_{oil} is the density of the pilot fuel.

2) The penetration distance of the pilot fuel, *l,* is calculated using the method from the *Cummins* gas-phase injection model, as shown in Equations 2 and 3.

$$l = F \cdot t^{0.6} \tag{2}$$

$$F = 450 d_{id}^{0.5} \left(\frac{\rho_{bpc}}{\rho_{oil}}\right)^{0.4} \left(\frac{\rho_{upc}}{\rho_{oil}}\right)^{0.5} \cdot \left(1 + \frac{\rho_{upc}}{\rho_a}\right)^{-0.82} \left(P_{id} - P_{pc}\right)^{0.25} \tag{3}$$

Where d_{id} is the nozzle diameter, ρ_{bpc} is the burned zone density in the pre-chamber, ρ_{upc} is the unburned zone density in the pre-chamber, and ρ_a is the air density.

3) The tip velocity of the pilot fuel, v_{jet}, is calculated using the method proposed by Ouellette et al. [17], as shown in Equation 4.

$$v_{jet} = \frac{1}{2} \cdot t^{-\frac{1}{2}} \left[2k_d \cdot v_{oil} d_{id} \left(\frac{\rho_{oil}}{\rho_{pc}}\right)^{\frac{1}{2}} \right]^{\frac{1}{2}} \tag{4}$$

Where t is the time, k_d is the model coefficient, and ρ_{pc} is the density in the pre-chamber.

4) The ignition delay, τ_{id}, is calculated using the method proposed by Assanis et al. [18], as shown in Equation 5.

$$\tau_{id} = 2.4 \phi^{-0.2} \cdot \bar{P}^{-1.02} \cdot \exp\left(\frac{E_a}{R_u * \bar{T}}\right) \tag{5}$$

Where ϕ is the equivalence ratio, $\bar{P}$ is the injection pressure, E_a is the activation energy, R_u is the ideal gas constant, and $\bar{T}$ is the injection temperature.

3.2.2 Pre-Chamber Combustion Process

1) The laminar flame speed, S_l, is calculated using the method proposed by Poinsot et al. [19], as shown in Equation 6.

$$S_l = S_0 * \left(\frac{T_u}{T_0}\right)^{aT} * \left(\frac{P}{P_0}\right)^{aP} \tag{6}$$

Where S_0 represents the initial velocity of the laminar flame, T_u is the temperature of the unburned zone, T_0 is the ambient temperature, P is the pressure, P_0 is the ambient pressure, aT is the temperature exponent, and aP is the pressure exponent.

2) The turbulence kinetic energy k in the pre-chamber is predicted using the *k-equation* model proposed by Ikegami [20], as shown in Equation 7.

$$\frac{d(mk)}{dt} = \eta_{jet} \cdot \frac{dm_{\text{oil}}}{dt} \cdot \frac{v_{jet}^2}{2} + \eta_{sw} \cdot m \cdot \frac{{u_{sw}}^3}{l_I} - m \cdot \frac{(2k/3)^{3/2}}{l_I} \tag{7}$$

Where m is the mass, η_{jet} is the fraction of jet kinetic energy converted into turbulence energy, dm_{oil}/dt is the pilot fuel mass flow rate, η_{sw} is the

fraction of swirl kinetic energy converted into turbulence energy, and l_l is the turbulence length scale. The swirl velocity u_{sw} satisfies Equation 8, where β is the injector arrangement angle.

$$u_{sw} = v_{jet} \cdot \cos(\beta) \tag{8}$$

3) During the initial injection phase, the mass of the unburned mixture entrained by the pilot fuel, dm_{en_oil}, is calculated using the momentum conservation law, as shown in Equation 9.

$$dm_{\mathrm{en\_oil}}^{k} = \frac{dm_{oil} \cdot v_{\mathrm{oil}} + m_{\mathrm{en\_oil}}^{k-1} \cdot v_{\mathrm{jet}}^{k-1}}{v_{\mathrm{jet}}^{k}} - m_{\mathrm{en\_oil}}^{k-1} - m_{\mathrm{oil}} \tag{9}$$

Where dm_{oil} is the injected pilot fuel amount per unit time, m_{en_oil} is the accumulated mass of the unburned mixture entrained by the pilot fuel, and m_{oil} is the total accumulated mass of the pilot fuel. After ignition, the mass of the mixture entrained by the pilot fuel, dm_{en}, is calculated as shown in Equation 10.

$$\mathrm{dm}_{en}^{k} = \rho_{upc} \cdot A_{f_{bpc}} \cdot \left(u_k + S_{lpc}\right) \tag{10}$$

Where $A_{f_{bpc}}$ is the combustion flame area in the pre-chamber, S_{lpc} is the laminar flame speed in the pre-chamber, and u_k is the root-mean-square velocity of turbulence energy in the pre-chamber, which can be derived from the turbulence kinetic energy k, as shown in Equation 11.

$$u_k = \sqrt{\frac{3}{2}k} \tag{11}$$

4) Based on the entrained mixture mass of pilot fuel and natural gas, the heat release rate in the pre-chamber, dQ_{pc}/dt, is calculated, as shown in Equation 12.

$$\frac{dQ_{pc}}{dt} = hu_{CH4} \cdot \frac{dm_{CH4}}{dt} + hu_{oil} * \frac{dm_{oil}}{dt} \tag{12}$$

Where hu_{CH4} and hu_{oil} are the lower heating values of natural gas and pilot fuel, respectively, and dm_{CH4} is the mass of burned natural gas.

3.2.3 Jet Flame Ignition and Entrainment Process

1) The velocity of the jet flame at the outlet of the connecting passage, v_{jet_mc}, is similarly determined using the Bernoulli equation, as shown in Equation 13.

$$v_{jet\_mc} = \sqrt{\frac{2 \cdot \left(P_{pc} - P_{mc}\right)}{\rho_{jet\_mc}}} \tag{13}$$

Where P_{mc} is the pressure in the main combustion chamber, and ρ_{jet_mc} is the density of the jet in the main combustion chamber.

2) The velocity of the jet flame tip, u_t, is given by Equation 14, where d_{noz} is the diameter of the connecting passage, and ρ_{mc} is the density in the main combustion chamber.

$$u_t = \frac{1}{2} \cdot t^{-\frac{1}{2}} \left[2k_d \cdot v_{jet\_mc} d_{noz} \left(\frac{\rho_{jet\_mc}}{\rho_{mc}} \right)^{\frac{1}{2}} \right]^{\frac{1}{2}} \tag{14}$$

Additionally, after the pre-chamber jet flame injection ends, the jet velocity will decay, and after a certain response time, τ_v, it will propagate to the jet flame tip [21, 22]. For this, the method proposed by Liu et al. [22] is used to calculate the decayed jet flame tip velocity, as shown in Equations 15 and 16, where C_j is the model coefficient, and l_{bmc} is the length of the jet flame in the main combustion chamber. This can be derived from the cone and sphere jet shape combined with the known jet flame volume, V_{bmc}.

$$u_t(\mathrm{t} + \Delta\mathrm{t}) = u_t(\mathrm{t}) + \left(v_{jet\_mc} - u_t(\mathrm{t})\right) \left(1 - \exp\left(\frac{-\Delta\mathrm{t}}{\tau_{\mathrm{v}}}\right)\right) \tag{15}$$

$$\tau_v = C_j \frac{l_{bmc}}{v_{jet\_mc}} \tag{16}$$

3) In the initial phase of the jet flame entering the main combustion chamber, the mass of the entrained mixture, dm_{en_jet}, is calculated based on the momentum conservation law, as shown in Equation 17.

$$dm_{en\_jet}^{k} = \frac{dm_{jet} \cdot v_{\mathrm{jet\_mc}} + m_{bmc}^{k-1} \cdot u_t^{k-1}}{u_t^{k}} - m_{bmc}^{k-1} - m_{jet} \tag{17}$$

Where m_{jet} is the total mass of the jet flame, and m_{bmc} is the mass of the burned region in the main combustion chamber.

3.2.4 Main Combustion Chamber Turbulent Entrainment Combustion Process

1) The turbulent combustion velocity, S_T, is calculated using the methods proposed by Gülder et al. [23] and Damköhler et al. [24], as shown in Equation 18.

$$\frac{S_T}{S_l} = 1 + C_{tur}\left(\frac{u'}{S_l}\right)^{0.5} \cdot \mathrm{Re}_T^{1/4} \tag{18}$$

Where C_{tur} is the model coefficient, u' is the root mean square velocity, and Re is the Reynolds number.

2) The mass of the entrained unburned mixture, dm_{en_tur}, is given by Equation 19. Where ρ_{umc} is the density of the unburned region in the main combustion chamber, and $A_{f_{bmc}}$ is the contact area between the burned and unburned regions in the main combustion chamber.

$$dm_{\mathrm{en\_tur}} = \rho_{umc} \cdot S_T \cdot A_{f_{\mathrm{bmc}}} \tag{19}$$

Furthermore, the turbulent entrainment of unburned premixed gas in the main combustion chamber is a typical premixed turbulent combustion process in a confined space. The combustion flame can be divided into several regions: the laminar flames, wrinkled flamelets, corrugated flamelets, thin reaction zones, and broken reaction zones [25, 26]. Most of the combustion occurs within the thin reaction zone, and this reaction zone is closely related to the laminar flame thickness [27, 28]. In this model, the turbulent flame entrains the premixed gas, and part of the premixed gas burns in a laminar manner on the Taylor microscale [29, 30].

Therefore, the mass of the unburned mixture that can be used for combustion during each time step, dm_{b_tur}, is given by Equation 20.

$$dm_{\mathrm{b\_tur}} = \frac{m_{\mathrm{en\_tur}} - m_{\mathrm{b\_tur}}}{\tau_b} \tag{20}$$

Where m_{b_tur} is the mass of unburned mixture that undergoes combustion after being entrained by the turbulent flame. The characteristic time for laminar flame combustion, τ_b , is calculated using Equations 21 and 22. Where λ_T is the Taylor microscale, C_{la} is the model coefficient, v_{kin} is the kinematic viscosity, k_{pmc} is the average turbulent kinetic energy in the main combustion chamber, and ε_{pmc} is the average dissipation in the main combustion chamber.

$$\tau_b = \frac{\lambda_T}{S_{lmc}} \tag{21}$$

$$\lambda_T = C_{la} \cdot \sqrt{\frac{v_{kin}}{k_{pmc} \cdot \varepsilon_{pmc}}} \tag{22}$$

3) The turbulent model in the main combustion chamber is given by Equation 23, where α_{mc}, C_T are model coefficients, and ε is the turbulent dissipation.

$$\frac{d(mk)}{dt} = \alpha_{mc}(1 - C_T) \cdot \frac{1}{2}\sum m_{jet} \cdot v_{jet\_mc}{}^2 + \eta_{sw} \cdot m \cdot \frac{u_{sw}{}^3}{l_I} - m\varepsilon \tag{23}$$

The strong swirl formed during the scavenging and compression processes promotes the formation of a uniform premixed gas from natural gas and air, and also influences the later stage of the jet flame's entrainment of the premixed gas. Therefore, the calculation of swirl velocity, u_{sw}, is based on the method proposed by Han et al. [31], considering angular momentum L_{swirl}, and accounting for angular momentum losses during scavenging and compression due to various reasons, including mass loss $L_{massloss}$, wall friction $L_{wallfriction}$, and shear in the swirl $L_{innershear}$, as shown in Equations 24 and 25. Where L_{in} is the angular momentum of the swirl formed by the fresh air and natural gas.

$$L_{swirl} = f\left(u_{sw}\right) \tag{24}$$

$$L_{swirl} = L_{in} - L_{massloss} - L_{wallfriction} - L_{innershear} \tag{25}$$

4) The total mass burned per time step, dm_{bmc}, and the total heat release rate in the main combustion chamber, dQ_{mc}/dt, are given by Equations 26 and 27, respectively, after coupling the jet flame entrainment and turbulent flame entrainment processes.

$$dm_{bmc} = dm_{en\_jet} + dm_{b\_tur} \tag{26}$$

$$\frac{dQ_{mc}}{dt} = hu \cdot \frac{dm_{bmc}}{dt} \tag{27}$$

3.2.5 Other Submodels

In addition to the submodels mentioned above, the entire combustion model also includes other submodels, such as the thermodynamic basic

differential equations that govern the entire calculation process, the ideal gas state equation, the ignition delay submodel, the working fluid property calculation submodel, the heat transfer submodel, and the instantaneous working volume calculation submodel for the cylinder. These will not be elaborated upon here.

4 MODEL VERIFICATION AND RESULT ANALYSIS

4.1 Model Verification

In order to verify the accuracy of the model, the results of the strong swirl combustion model were compared with experimental data and CFD simulation results. As shown in Figure 6, the predicted cylinder pressure peak and the trend of variation by the model match well with the experimental data.

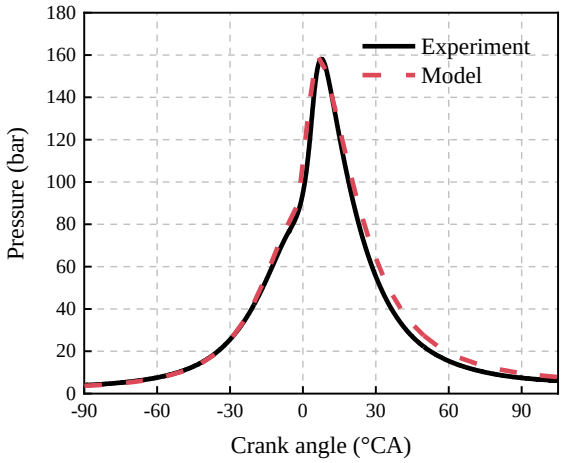

Figure 6. Comparison of model cylinder pressure and experimental cylinder pressure.

Due to the small volume of the pre-chamber and the difficulty in measurement, the pre-chamber pressure calculated by the model is validated against the CFD results, as shown in Figure 7. Overall, there is good consistency between the two, but there are still some differences. This is considered to be due to the detailed description of processes such as fuel atomization and evaporation in the CFD simulation, whereas these processes are neglected in the phenomenological model, which assumes that the fuel is injected in a gaseous phase.

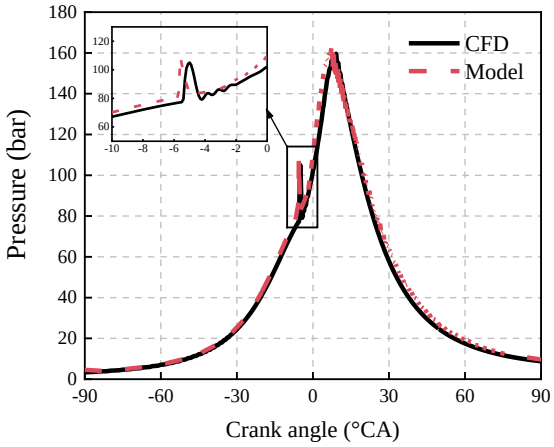

Figure 7. Comparison of model and CFD pre-chamber cylinder pressure.

Figure 8 shows the temperatures of the unburned and burned regions in the main combustion chamber, as well as the final average temperature, i.e., the main combustion chamber temperature. This result was also compared with CFD results, and it can be seen that both match well, with the peak values corresponding to nearly identical crankshaft angles, as shown in Figure 9.

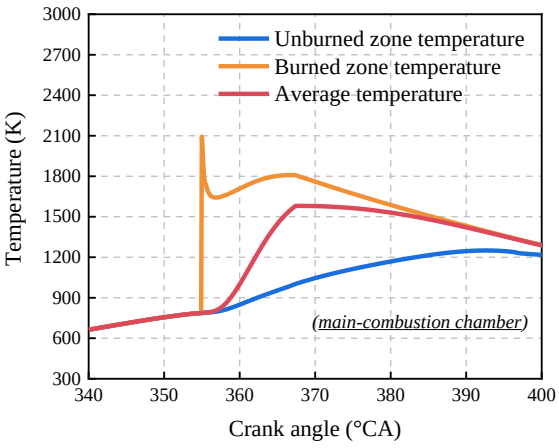

Figure 8. Temperatures of the unburned, burned, and average zones in the main combustion chamber.

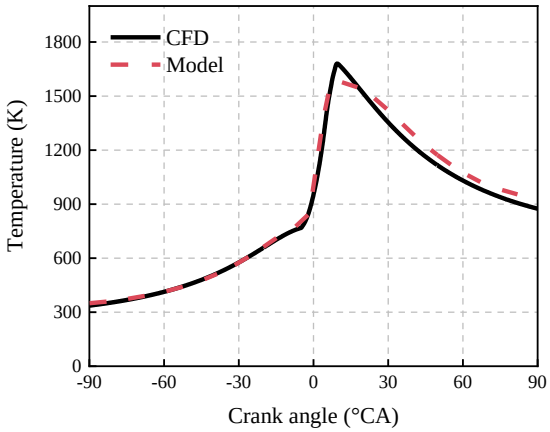

Figure 9. Comparison of model and CFD temperature results.

4.2 Model Result Analysis

4.2.1 The Effect of Initial Turbulent Kinetic Energy on the Combustion Process

To investigate the effect of the initial turbulent kinetic energy on the combustion process, six different initial turbulent kinetic energy values were selected: 11.6, 11.8, 12.2, 12.8, 13.3, and 13.8. As shown in Figure 10, as the initial turbulent kinetic energy increases, the peak value of entrainment mass in stage a also increases. Although the trend is opposite in stage b, the overall mass still increases, which leads to an increase in cylinder pressure and pressure rise rate, as shown in Figures 11 and 12.

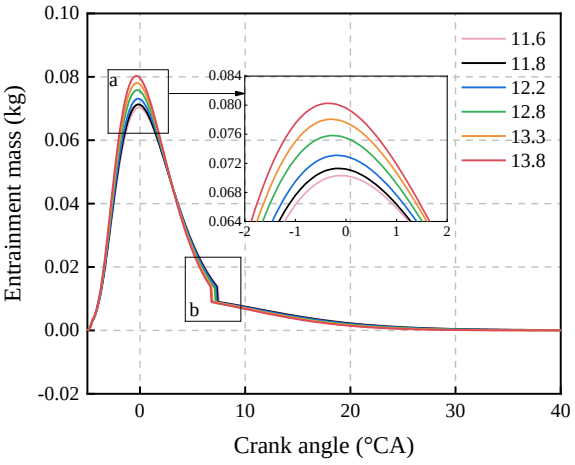

Figure 10. Entrainment mass for different initial turbulent kinetic energies.

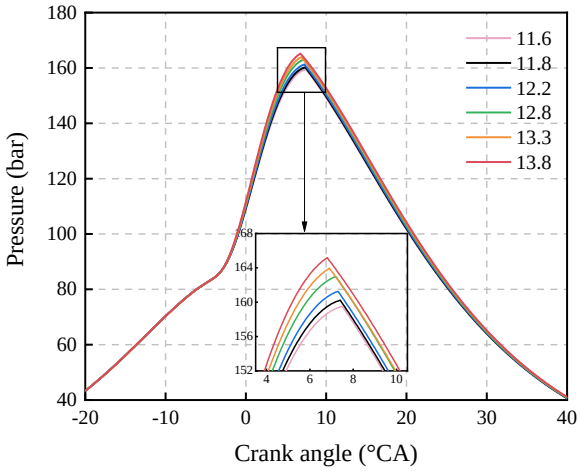

Figure 11. Cylinder pressure for different initial turbulent kinetic energies.

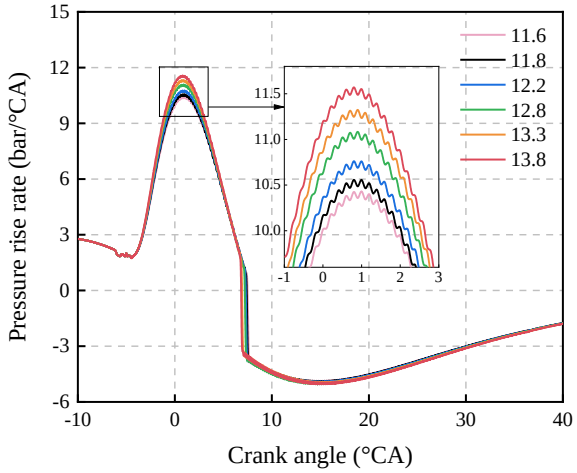

Figure 12. Pressure rise rate for different initial turbulent kinetic energies.

5 CONCLUSIONS

Based on experimental data and observations from CFD simulation results, this study has developed a reduced-dimension strong swirl combustion phenomenological model for the pre-chamber natural gas low-pressure injection dual-fuel engine and has validated it.

(1) The jet flame entering the main combustion chamber entrains unburned premixed gas under the influence of high-speed jets and strong swirls. The swirl behavior is analyzed based on the loss of angular momentum.

(2) The initial turbulent kinetic energy directly affects the entrainment mass of the mixed gas, which in turn influences the heat release rate and cylinder pressure, ultimately affecting the combustion process.

6 ACKNOWLEDGMENTS

This research was financially supported by the National Natural Science Foundation of China (Grant No. 52301367).

7 REFERENCES AND BIBLIOGRAPHY

[1] Wu, Y., Liu, L., Liu, B., Cao, E. and Xiong, Q. 2023. Investigation of rapid flame front controlled knock combustion and its suppression in natural gas dual-fuel marine engine. *Energy*, 279, 128078.

[2] Haider, S., Meyer, K. E., Schramm, J. and Mayer, S. 2010. PIV Study of the Effect of Piston Motion on the Confined Swirling Flow in the Scavenging Process in 2-Stroke Marine Diesel Engines. *In 26th CIMAC World Congress*, Bergen, p:270.

[3] Ingvorsen, K. M., Meyer, K. E., Walther, J. H. and Mayer, S. 2013. Turbulent swirling flow in a model of a uniflow-scavenged two-stroke engine. *Experiments in fluids*, 54, 1-17.

[4] Ingvorsen, K. M., Meyer, K. E., Walther, J. H. and Mayer, S. 2014. Turbulent swirling flow in a dynamic model of a uniflow-scavenged two-stroke engine. *Experiments in fluids*, 55, 1-18.

[5] Nishimoto, K. and Kamimoto, T. 1984. A study on the influence of inlet angle and Reynolds number on the flow-pattern of uniflow scavenging air. *SAE transactions*, 788-797.

[6] Liu, D., OGALO, D.O. and Liu, L. 2021. Study on Phenomenological Spray Model of the Effect of Coupling Swirl Flow in Low-Speed Two-Stroke Marine Diesel Engines. *Chinese Internal Combustion Engine Engineering*, 42(2), 1-8.

[7] Tunç, G. 2025. Swirl number effects on combustion characteristics of oxygen-enriched methane-hydrogen fuel mixture under acoustic excitation conditions. *International Journal of Hydrogen Energy*, 101, 1014-1028.

[8] Jeon, Y., Nam, H. T. and Lee, S. 2024. Combustion and emission characteristics for various swirler geometries and fuel heating values in a premixed low swirl combustor system. *Energy*, 131986.

[9]Hu, J., Pei, Y., An, Y., Zhao, D., Zhang, Z., Sun, J.and Gao, D. 2023. Study of active pre-chamber jet flames based on the synergy of airflow with different nozzle swirl angle. *Energy*, 282, 128198.

[10] Lu, Y., Wei, M., Wang, X., Ji, Q., Ao, C., Wang, X. and Liu, J. 2024. Numerical study on influences of intake temperature and swirl ratio on in-cylinder combustion and pollutant formation characteristics of ammonia/diesel dual-fuel engine. *Journal of the Energy Institute*, 117, 101860.

[11] Ye, Y., Liu, H., Li, J., Liu, T., Dong, J., Liu, B. and Yao, M. 2023. A numerical investigation on the effects of intake swirl and mixture stratification on combustion characteristics in a natural-gas/diesel dual-fuel marine engine. *Journal of Thermal Science*, 32(1), 414-426.

[12] Liu, L., Wu, Y., Xiong, Q. and Liu, T. 2019. Analysis on flow motion and combustion process in pre-chamber and main chamber for low-speed two-stroke dual-fuel engine. SAE Technical Paper. (No. 2019-01-2175).

[13] Bondarenko, O. and Fukuda, T. 2020. Development of a diesel engine's digital twin for predicting propulsion system dynamics. *Energy*, 196, 117126.

[14] Stoumpos, S., Theotokatos, G., Mavrelos, C. and Boulougouris, E. 2020. Towards marine dual fuel engines digital twins—integrated modelling of thermodynamic processes and control system functions. *Journal of Marine Science and Engineering*, 8(3), 200.

[15] Van Dinter, R., Tekinerdogan, B. and Catal, C. 2022. Predictive maintenance using digital twins: A systematic literature review. *Information and Software Technology*, 151, 107008.

[16] Liu, L., Wen, X., Xiong, Q. and Ma, X. 2019. Phenomenological Modeling of Combustion in Pre-Chamber and the Pilot Flame for Natural Gas Engines. *In Internal Combustion Engine Division Fall Technical Conference* (Vol. 59346, p. V001T06A005). *American Society of Mechanical Engineers.*

[17] Ouellette, P. and Hill, P. G. 2000. *Turbulent transient gas injections*. J. Fluids Eng., 122(4): 743-752.

[18] Assanis, D. N., Filipi, Z. S., Fiveland, S. B., et al. 2003. A predictive ignition delay correlation under steady-state and transient operation of a direct injection diesel engine. *J. Eng. Gas Turbines Power*, 125(2): 450-457.

[19] Poinsot, T. and Veynante, D. 2005. *Theoretical and numerical combustion*[M]. RT Edwards, Inc.

[20] Ikegami, M., Shioji, M. and Koike, M. 1985. A stochastic approach to model the combustion

process in direct-injection diesel engines. *In Symposium (International) on Combustion* (Vol. 20, No. 1, pp. 217-224).

[21] Musculus, M. P. and Kattke, K. 2009. Entrainment waves in diesel jets. *SAE International Journal of Engines*, 2(1), 1170-1193.

[22] Liu, L., Peng, Y., Ma, X., et al. 2019. Phenomenological modeling of diesel spray with varying injection profile[J]. *Proceedings of the Institution of Mechanical Engineers, Part D: Journal of Automobile Engineering*, 233(11): 2780-2790.

[23] Gülder, Ö. L. 1991. Turbulent premixed flame propagation models for different combustion regimes[C]. *Symposium (International) on Combustion*, 23(1): 743-750.

[24] Damköhler, G. 1940. Der einfluss der turbulenz auf die flammengeschwindigkeit in gasgemischen[J]. *Zeitschrift für Elektrochemie und angewandte physikalische Chemie*, 46(11): 601-626.

[25] Peters, N. 2000. *Turbulent Combustion*. Cambridge: Cambridge University Press.

[26] Sun, M. B., Bai, X. S. and Wang, G. Z. 2015. *Flamelets Theory and Application for Turbulent Combustion* (in Chinese). Beijing: Science Press.

[27] Ye, Y., Yue, Z., Wang H, et al. 2021. A Mapping Approach for Efficient CFD Simulation of Low-Speed Large-Bore Marine Engine with Pre-Chamber and Dual-Fuel Operation[J]. *Energies*, 14(19): 6126.

[28] Cernik, F., Macek, J., Dahnz, C., et al. 2016. Dual fuel combustion model for a large low-speed 2-stroke engine[R]. *SAE Technical Paper* (No. 2016-01-0770).

[29] Blizard, N. C. and Keck, J. C. 1974. Experimental and theoretical investigation of turbulent burning model for internal combustion engines[J]. *SAE Transactions*, 846-864.

[30] Tabaczynski, R. J., Ferguson, C. R. and Radhakrishnan, K. 1977. A turbulent entrainment model for spark-ignition engine combustion[J]. *SAE transactions*, 2414-2433.

[31] Han, X., Liu, D., Liu, L., et al. 2024. Research on Scavenging Flow Dynamics of Marine Two-Stroke Engines With a CFD-Derived Quasi-Dimensional Model[J]. *International Journal of Engine Research*, 25(8):1611-1622.